The Most Effective Remote Forcing in Causing U.S.-Wide Heat Extremes as Revealed by CESM Green's Function Experiments

Yutian Wu[1] [ID]**, Jian Lu[2]** [ID]**, Mingfang Ting[1]** [ID]**, Richard Seager[1]** [ID]**, and Fukai Liu[3]**

[1]Lamont-Doherty Earth Observatory of Columbia University, Palisades, NY, USA, [2]Pacific Northwest National Laboratory, Richland, WA, USA, [3]Ocean University of China and Qingdao National Laboratory for Marine Science and Technology, Qingdao, China

Abstract We make use of the Community Atmosphere Model version 5 Green's function q-flux perturbation experiments to explore the most effective remote forcing in driving U.S.-wide summer heat extremes. We find that positive q-flux forcing over the western North Pacific Ocean is the most effective in causing an increased heat extreme frequency. This works by driving increased sea surface temperature and precipitation over western North Pacific and an eastward propagating Rossby wave train with an anomalous ridge over the contiguous U.S. In comparison, negative q-flux forcing over the eastern tropical Pacific and its resulting surface cooling also leads to an increased heat extreme frequency but is less effective. Furthermore, guided by the Green's function results, we separate the role of western North Pacific warming and eastern tropical Pacific cooling in U.S. heat extremes in prescribed sea surface temperature experiments and ERA5 reanalysis data and find overall consistent conclusions.

Plain Language Summary We study summertime U.S. heat extremes and their precursors in ocean surface forcing. Using a novel approach, we find that western North Pacific warming and wetting is the most effective way to cause an increased frequency of U.S.-wide heat extremes. In comparison, eastern tropical Pacific cooling can also lead to an increased heat extreme frequency but is less effective. Our work advances understanding of U.S. heat extremes with important implications for their predictability.

1. Introduction

Heat extremes are a natural component of the climate system but have become more intense, more frequent, and more spatially extensive as a result of a warming climate (Meehl & Tebaldi, 2004; Perkins-Kirkpatrick & Lewis, 2020). Heat extremes are also closely related to other compound climate extremes, such as droughts (e.g., H. Wang et al. (2014)), wildfires (e.g., P. Williams et al. (2013)) and air pollution (e.g., Schnell et al. (2016); Shen et al. (2016)), causing widespread agricultural, ecosystem and societal impacts. Previous work has extensively studied the precursors of heat extremes including persistent anticyclones (e.g., Dole et al. (2011); Trenberth and Fasullo (2012)) and local land-atmosphere feedbacks (e.g., Fischer et al. (2007); Lorenz et al. (2010); Mueller and Seneviratne (2012)).

Multiple remote factors play an important role in affecting U.S. heat extremes during boreal summer. Previous studies have found that tropical (Deng et al., 2018; Hoerling & Kumar, 2003; Lee & Grotjahn, 2019; Lin et al., 2022; Lopez et al., 2022; Schubert et al., 2004) and midlatitude (Namias, 1982; Namias, 1991; Lyon & Dole, 1995; B. Wang et al., 2001; Lau et al., 2005; Ding et al., 2011; Donat, 2016; McKinnon et al., 2016; Zhu & Li, 2016; Lopez et al., 2019; Jong et al., 2020) sea surface temperature (SST) anomalies can precede extreme heat events. Typically these SST anomalies generate a poleward and eastward propagating Rossby wave train pattern and establish a high pressure system in the U.S., which is favorable for the occurrence of heat extremes. For example, Hoerling and Kumar (2003) attributed the drought/heat conditions in the U.S. to cold SSTs in the eastern tropical Pacific and warm SSTs in the western tropical Pacific and Indian Ocean. McKinnon et al. (2016) studied the heat extremes in the eastern U.S. and found a skillful prediction by as much as 50 days in advance from the Pacific Extreme Pattern with a zonal tripole pattern in the midlatitude Pacific SST (i.e., a cold-warm-cold SST pattern). However, the impact of the tropical and midlatitude SSTs could be hard to disentangle in nature due to their coupling. In addition, a quasi-stationary midlatitude circumglobal teleconnection pattern, likely

driven by midlatitude internal dynamics, can also drive U.S. heat extremes (Petoukhov et al., 2013; Screen & Simmonds, 2014; Teng et al., 2013).

Considering that many remote factors could contribute to increased U.S. heat extremes, a key question we aim to address here is—what is the most effective remote oceanic forcing in driving U.S. heat extremes in summer? To answer this question, we make use of a set of Green's function q-flux perturbation experiments, construct the linear response function (LRF) that explicitly and causally links U.S. heat extreme response to ocean q-flux forcing and compute the pair of response and forcing that is associated with the largest response-to-forcing ratio. As shown in more details below, the Green's function approach is useful in identifying a causal relationship between the forcing and response, as compared to conventional statistical methods.

2. Data and Methods

2.1. Model Experiments and Reanalysis Data Sets

First, we make use of the Green's function q-flux perturbation experiments by Liu et al. (2018). The experiments are performed using the slab ocean model (SOM) configuration of the CESM1.1 (Hurrell et al., 2013) which includes the Community Atmosphere Model version 5 (CAM5) (2.5° longitude by 1.9° latitude horizontal resolution) and a thermodynamic sea ice component of the Community Ice Code (CICE). The control simulation is a 900-year long CESM1.1-SOM run, forced with pre-industrial carbon dioxide levels and solar radiation, with a specified climatological ocean mixed layer depth h and q-flux that represents the three-dimensional ocean heat transport divergence and mixing. The SST is prognostic and calculated based on the thermal coupling between the SOM and the atmosphere. For the perturbation experiments, 97 pairs of localized "warm patch" and "cold patch" simulations are performed, in which an anomalous elliptical q-flux patch (Figure S1 in Supporting Information S1) is added to or subtracted from the climatological q-flux. More details on the experimental design can be found in Liu et al. (2018). 200-year daily surface temperature (TS) from the control and 40-year daily TS from each of the perturbation experiments are used for the analysis of heat extremes.

For observations, we use the European Centre for Medium-Range Weather Forecasts (ECMWF) ERA5 reanalysis (Hersbach et al., 2020) due to its long time span (1959–2021) as compared to other reanalysis datasets. We remove the linear trend in ERA5 for the analysis. In addition, we also use the prescribed SST global Atmospheric Model Intercomparison Project (AMIP) ensembles forced with observational SST and sea ice with CAM5.2 and CAM6 that are performed by NCAR. For CAM5.2 with a horizontal resolution of 1.25° longitude by 0.9° latitude, we focus on 1959–2015, remove the linear trend and aggregate the data over 10 ensemble members, and in total we have 570 years. Similarly for CAM6, which has the same horizontal resolution as CAM5.2, we have 630 years (1959–2021, 10 ensemble members). We use post-1959 data in prescribed SST runs to match the ERA5 time span.

2.2. Linear Response Function

We use the linear response function (LRF) method to extract the most effective q-flux forcing that drives U.S. heat extremes from the Green's function experiments. A dynamical climate system can be formulated as (Palmer, 1999):

$$\dot{\mathbf{x}} = \mathbf{L}\mathbf{x} + \mathbf{A}\mathbf{f}, \tag{1}$$

where $\mathbf{x}$ denotes the response in state variables in the climate system, $\mathbf{f}$ represents the external forcing, $\mathbf{L}$ is the LRF that represents the dynamical climate system response to the forcing and is a square matrix, and $\mathbf{A}$ works to bridge the forcing to the response and could be a non-square matrix if the forcing and response are different variables and have different spatial coverage. Since we focus on the equilibrium response, $\dot{\mathbf{x}} = \mathbf{0}$ and Equation 1 can be written as

$$\mathbf{A}^{-1}\mathbf{L} = -\mathbf{f}\mathbf{x}^{-1}. \tag{2}$$

We define $\tilde{\mathbf{L}} = \mathbf{A}^{-1}\mathbf{L}$ and $\tilde{\mathbf{L}}$ plays a similar role as the LRF $\mathbf{L}$ as in the literature. We calculate $\tilde{\mathbf{L}}$ by using Equation 2 and the Green's function experiments. Specifically, $\mathbf{f}$ is the q-flux forcing perturbation across all the perturbation experiments and has $M \times J$ dimension with M representing the number of grid points over the ocean

covered by q-flux and J representing the number of perturbation experiments. And, as the linear component approximates the actual response when the forcing is small (Gritsun, 2010), we focus on the linear component of the U.S. heat extreme response by estimating $\mathbf{x} = (\mathbf{x}_+ - \mathbf{x}_-)/2$ with subscripts $+$ and $-$ denoting the positive and negative forcing experiments, respectively, across all the perturbation experiments. Although it's not the focus of this study, the nonlinear response is non-negligible (not shown). $\mathbf{x}$ has a dimension of $N \times J$ with N indicating the number of grid points covering the contiguous U.S. Since $\mathbf{x}$ is not necessarily a square matrix, we calculate $\mathbf{x}^{-1}$ using pseudo-inversion as $(\mathbf{x}^{\mathbf{T}}\mathbf{x})^{-1}\mathbf{x}^{\mathbf{T}}$, where superscript $\mathbf{T}$ denotes transpose, and $\mathbf{x}^{\mathbf{T}}\mathbf{x}$ is found to be well-conditioned and invertible in our study. Thus $\tilde{\mathbf{L}}$ has $M \times N$ dimension, independent of the number of experiments. Then the singular value decomposition of $\tilde{\mathbf{L}}$ is calculated, and the most effective forcing and its corresponding response is provided by the pair of singular vectors associated with the smallest singular number and thus maximum response-to-forcing ratio (Barsugli & Sardeshmukh, 2002; Dong et al., 2019; Goodman & Marshall, 2002; Hassanzadeh & Kuang, 2016; Liu et al., 2018; Lu et al., 2020; Marshall & Molteni, 1993; Wu et al., 2021). The right singular vector, known as the neutral vector, reveals the most excitable mode of the response, and the left singular vector, which corresponds to the optimal forcing, is the most effective q-flux forcing in driving the response. The other variables ($\mathbf{Z}$, such as surface temperature and precipitation) associated with the neutral vector and optimal forcing can be estimated as $\mathbf{Z}_n \approx \mathbf{Z}\mathbf{x}^{-1}\mathbf{x}_n$ with subscript n denoting the neutral vector.

In addition, we focus on extreme heat frequency and define it as the number of days exceeding the 95th percentile of the daily surface temperature threshold. For the linear response of extreme heat frequency, we first calculate the 95th percentile based on the 200-year control run. We then calculate the heat frequency separately in the positive and negative forcing runs and take the difference between the two divided by 2. We focus the analysis on the contiguous U.S., which is the land area in the region of 125°–67°W, 25°–49°N.

3. Results

3.1. Green's Function Experiment Results

Figures 1ab show the neutral vector of U.S. extreme heat frequency and corresponding optimal q-flux forcing that is the most effective in exciting a U.S. wide and seasonally increased extreme heat frequency. The optimal forcing is first scaled by the smallest singular number. Then both the neutral vector and optimal forcing are scaled so that the maximum of the neutral vector over the U.S. is 6 days so as to better compare with the rest of the study. For the neutral vector, it shows an increase of extreme heat frequency broadly over the entire U.S. by about 2–6 days in summertime mean, especially in the South and the West. For the optimal q-flux forcing, positive values indicate that a positive forcing causes an overall increased U.S. extreme heat frequency while negative values indicate that a negative forcing leads to an overall increased extreme frequency. The magnitude measures the covariability between the optimal forcing and neutral vector, a forcing that projects more strongly on the optimal forcing pattern (Figure 1b) tends to drive a larger magnitude of the heat frequency pattern (Figure 1a). The optimal q-flux forcing shows an overall positive forcing over the North Pacific and North Atlantic Ocean, a negative forcing in the eastern tropical Pacific and patchy patterns in the Southern Hemisphere oceans.

Since the q-flux perturbation is expected to affect the SST, which changes the diabatic heating, atmospheric teleconnection and thus heat extremes, Figures 1c, 1d, and 1e show these variables that are associated with the neutral vector to better reveal the linkage between the neutral vector and optimal forcing. The surface temperature associated with the optimal forcing shows an overall increase in most of the global ocean, particularly the North Pacific Ocean, the North Atlantic Ocean and the Southern Hemisphere oceans, and a relatively weaker cooling in the tropical eastern and central Pacific. The precipitation shows an increase in the NH subtropical western Pacific and midlatitude western Atlantic, an overall decrease in the Indian Ocean and tropical Pacific, and an overall increase in the northern tropical Atlantic. The 200 hPa geopotential height shows a nearly circumglobal wave train pattern in the NH midlatitudes, dominated by zonal wave number 4, 5, and 1, with a ridge over the midlatitude western Pacific, midlatitude eastern Pacific, contiguous U.S., midlatitude North Atlantic, and southeastern Europe. The results suggest that the warming over the North Pacific and its resulting increased precipitation likely drives a Rossby wave train and a summertime ridge over the contiguous U.S., which is favorable for heat extremes. The warming over the North Atlantic could also play a role and will be discussed next.

To better understand the LRF results, we perform a simple composite analysis based on the linear response by selecting the perturbation experiments with the 15 largest (Figure 2 left column) and 15 smallest (Figure 2
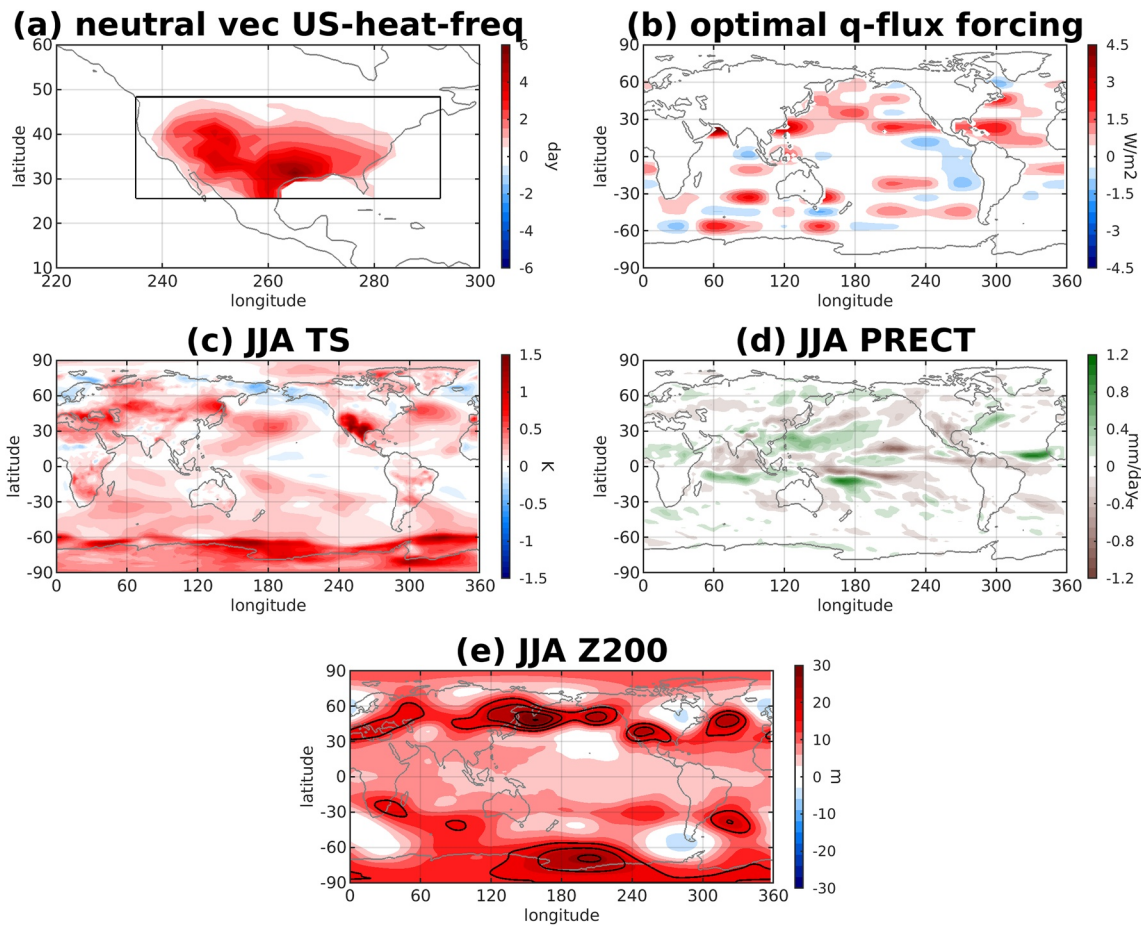
Figure 1. Linear response function results for summertime (JJA) U.S. extreme heat frequency. (a) The neutral vector for JJA U.S. extreme heat frequency and (b) its corresponding optimal *q*-flux forcing. The associated JJA (c) surface temperature (TS), (d) precipitation (PRECT), and (e) 200 hPa geopotential height (Z200 with contours starting from 15 m with an interval of 5 m) with the neutral vector. The neutral vector is scaled so that its maximum over the U.S. is 6 days. The optimal forcing is scaled by the smallest singular number and also the neutral vector rescaling. Box in (a) indicates the contiguous U.S.

right column) U.S.-mean extreme heat frequency response, respectively. Figure S2 in Supporting Information S1 shows the histogram of the linear response of U.S.-mean extreme heat frequency among the q-flux perturbation experiments. As can be seen, the 15 largest experiments correspond to the positive q-flux forcings leading to an increased heat frequency while the 15 smallest ones are the positive q-flux forcings causing a decreased heat frequency. Since the responses are linear, we flip the sign of Figure 2 right column so that negative q-flux forcing corresponds to an increased extreme heat frequency. The resultant q-flux forcing can be compared with the optimal forcing pattern in Figure 1b, while the physical consistency across the variables shown in the right panels of Figure 2 can be still maintained. As can be seen, Figures 2c and 2d in combination are similar to Figure 1b in pattern (i.e., the pattern correlation between Figure 1b and sum of Figures 2c and 2d is 0.66) and verify the LRF results, despite the difference in values. The LRF method takes the magnitude and pattern of extreme heat frequency into account while the composite analysis is a simple average. Nonetheless some features of the LRF results can be interpreted using the composite analysis. In particular, the composite analysis separates the optimal q-flux forcing into Figure 2c, which is dominated by positive q-flux forcings over the western and central North Pacific and western North Atlantic, and Figure 2d, which shows negative q-flux forcings over the eastern tropical Pacific and others scattered in the North Atlantic, Indian Ocean and Southern Ocean.

The associated atmospheric circulation in the composite means is also shown (Figures 2e–2l). Since localized q-flux forcing could drive a global surface temperature response, we test the robustness of the surface temperature response by examining the sign agreement in the composite. As a result of the positive q-flux forcings in Figures 2c and 2a net energy flux input into the atmosphere, the surface temperature (Figure 2e)
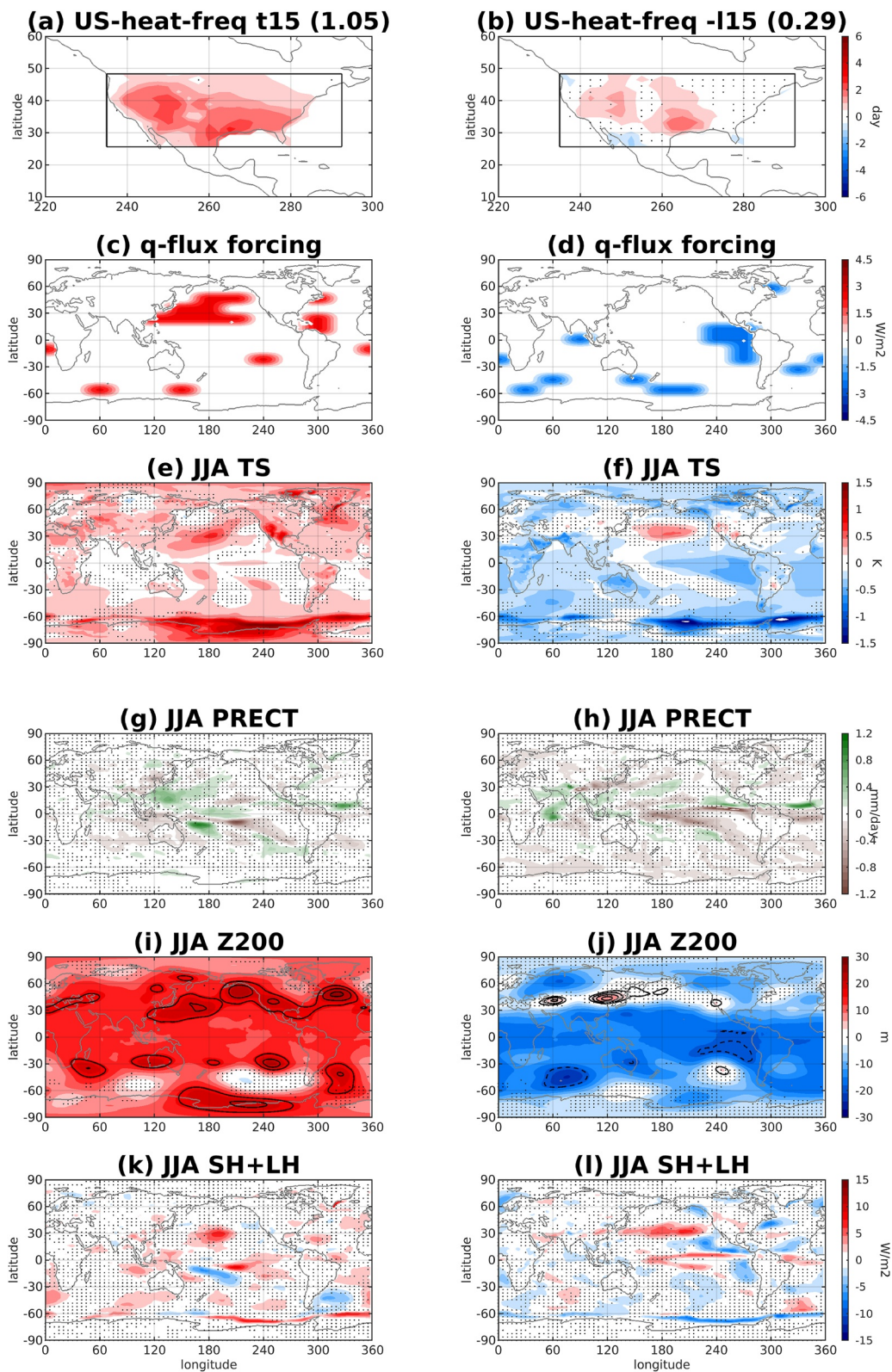
Figure 2.

shows a global warming. Similarly for Figures 2d and 2f, it shows a global cooling. Taking Figures 2e, 2g, & 2i all together, the positive q-flux forcings in Figure 2c drive an increased surface temperature and precipitation over the western North Pacific and an eastward propagating Rossby wave train that likely originates from the western North Pacific as a result of increased precipitation and has upper-level ridges south of Alaska and over the contiguous U.S. In the North Pacific Ocean, increased SST warming is generally co-located with increased precipitation and an upward turbulent heat flux anomaly (Figure 2k) indicating SST driving the atmosphere. For the North Atlantic, although a pronounced increased surface temperature is found in mid-and-high latitudes, in the q-flux experiments it lacks robustness in the composite and is thus not further discussed in this study although previous studies such as Lopez et al. (2022) found the tropical North Atlantic warming to be important for the Great Plains heat waves. On the other hand, the atmospheric circulation associated with Figure 2d shows a La Nina-like SST and precipitation in the tropical Pacific and North Pacific, in addition to an overall global cooling (Figures 2f, and 2h). This causes a ridge anomaly over the west of the U.S. (Figure 2j), leading to a modest increased heat frequency in the West and the South (Figure 2b). The turbulent flux response (Figure 2l) is overall consistent with a La Nina-like pattern. We note that the Southern Hemisphere q-flux forcing experiments are challenging to interpret but some of them possibly drive an increase of heat frequency by modifying the tropical and Northern Hemisphere SSTs.

The impact of western North Pacific warming and wetting on U.S. heat extremes has been explored in previous studies (B. Wang et al., 2001; Zhu & Li, 2016; Lopez et al., 2019). In particular, the underlying dynamical mechanism has been well studied in Lopez et al. (2019) using a simple linear baroclinic model forced by East Asian monsoon diabatic heating. Our precipitation pattern (Figures 1d and 2g) is similar to their East Asian monsoon rainfall (Figure 5ab of Lopez et al. (2019)). Our wave train pattern (Figures 1e and 2i) over the North Pacific sector is also similar to Figure 3bd of Lopez et al. (2019), especially the three upper-level ridges over the western North Pacific, the Aleutian low region, and the contiguous U.S. Our wave train pattern also extends to the North Atlantic and Europe and shares some resemblance to the circumglobal teleconnection in Teng et al. (2013). Our results differ from the Pacific Extreme Pattern in McKinnon et al. (2016) which found a zonal tripole pattern in the midlatitude Pacific SST in leading to eastern U.S. heat extremes in observations. One possibility underlying the difference may be the area of interest—while McKinnon et al. (2016) focused on the eastern U.S., our study is on U.S.-wide heat extremes.

In nature North Pacific warming can be caused by eastern tropical Pacific cooling on inter-annual timescales, making it challenging to disentangle their contributions. The Green's function experiments have the advantage in establishing the causal relationship between the forcing and response and in separating the effect of eastern tropical Pacific cooling and North Pacific warming on U.S. heat extremes. Comparing the left and right columns of Figure 2, it is clear that although both Figures 2c and 2d lead to an increased U.S. heat extreme frequency, the western North Pacific is more effective in causing a larger magnitude of increase averaged across the U.S. (about 1.05 days) than the eastern tropical Pacific (about 0.29 days). This also explains the dominance of North Pacific warming over eastern tropical Pacific cooling in causing the U.S. heat extremes as revealed by the LRF method (Figures 1b and 1c).

3.2. Support From Observations and Model Experiments

Next we explore whether there is any support for the LRF results in comprehensive model experiments and observations. Guided by the LRF results, we aim to separate the effect of western North Pacific warming in the absence of eastern tropical Pacific cooling and eastern tropical Pacific cooling on U.S. heat extreme frequency using composite analysis despite the caveat that cause-and-effect might be less clear. For the effect of North Pacific warming as revealed by Figure 2 left column, the fact that the SST is important in driving the atmosphere suggests that atmospheric models with prescribed SSTs may be able to simulate the teleconnection pattern. However,

Figure 2. Composite analysis of U.S. heat extreme frequency from Green's function q-flux experiments. (Left) Composite mean of the perturbation experiments that have the 15 largest U.S.-averaged heat extreme frequency. (Right) Similar to left but with the 15 smallest U.S.-averaged heat extreme frequency. All the variables in the right column are multiplied by −1 so that a negative q-flux forcing corresponds to an increase of U.S. heat extreme frequency. (a) U.S. heat extreme frequency, with the number within parentheses indicating the U.S.-averaged heat extreme frequency response. (c, e, g, i, k) Associated q-flux forcing perturbation, JJA surface temperature (TS), precipitation (PRECT), 200 hPa geopotential height (Z200), and sum of surface sensible (SH) and latent heat flux (LH) (positive upward from the surface to the atmosphere). Boxes in (a, b) indicate the contiguous U.S. For (a, b, e–l), grid points with less than 10 out of 15 experiments agreeing on the sign of the response are dotted. For (i, j), contours also plot Z200 with positive values in solid contours and negative values in dashed contours. In (i), the contours start from 16 m with an interval of 4 m. In (j), solid contours start from 2 m with an interval of 2 m, and dashed contours start from −20 m with an interval of −20 m.

we also note that the Green's function and prescribed SST experiments might not be directly comparable as the composites of the Green's function experiments include a net energy flux input (or output) into the atmosphere and thus a global warming (or cooling) due to experimental design.

We start by showing the results in prescribed SST experiments from CAM5.2, a similar model version to that in which the Green's function experiments are performed but with a finer horizontal resolution. To isolate the effect of western North Pacific warming in the absence of eastern tropical Pacific cooling, guided by Figures 2e and 2a composite of 60 years (which is the same 6 years in 10 ensembles, see Text S1 in Supporting Information S1 for detailed information) is made by conditioning on a warmer-than-normal western North Pacific (i.e., box-averaged temperature larger than 0.5 standard deviation) and a normal eastern tropical Pacific temperature (i.e., box-averaged temperature within $\pm$0.5 standard deviation). The box region of the western North Pacific is chosen based on Figures 2e, 2g, and 2i to isolate the localized warming and wetting in the western part. The box region of the eastern tropical Pacific is similar to the Niño 3.4 index region except for an extension in latitude to connect seamlessly with the western North Pacific box region. The results are overall insensitive to the choice of box region (not shown). The composite selection criterion is chosen to provide an adequate composite size but the conclusions remain the same with different criteria (Figure S3 in Supporting Information S1). As a result of warmer (Figure 3a) and wetter (Figure 3c) western North Pacific, an eastward propagating Rossby wave train is generated and leads to a ridge over the contiguous U.S. (Figure 3a) and an increased U.S.-wide heat extreme frequency by as large as 6 days in the JJA mean (Figure 3e), which is in agreement with the Green's function results.

For comparison, we also isolate the effect of eastern tropical Pacific cooling from CAM5 prescribed SST experiments making a composite of similar size in which the eastern tropical Pacific is colder-than-normal (i.e., box-averaged temperature less than -1 standard deviation). As shown in Figures 3b, 3d, and 3f, a typical poleward and eastward propagating wave train, which is similar to observations (e.g., Figure 3cf of Jong et al. (2020)), is generated following decreased surface temperature and precipitation in the eastern tropical Pacific Ocean, resulting in a ridge anomaly over eastern North America and an increased heat extreme frequency over the northeast U.S. by about 0.5–1.5 days in the summertime mean with limited region of statistical significance. A significant decrease of heat frequency is also found in the west. Therefore, the CAM5 prescribed SST experiments also suggest that western North Pacific warming plays a more important role in contributing to U.S. heat extreme frequency increase compared to eastern tropical Pacific cooling, in agreement with the Green's function results. However, the 200 hPa geopotential height and U.S. heat extreme frequency associated with eastern tropical Pacific cooling in the prescribed SST experiments are quite different from the Green's function composite analysis. This could be due to the global cooling and/or more complex remote SST response in the Green's function q-flux experiments.

Next we also extend our analysis to CAM6 prescribed SST experiments to explore possible model dependency. Overall the results are consistent with the LRF and CAM5 prescribed SST analysis that a warmer-than-normal western North Pacific in the absence of eastern tropical Pacific cooling is associated with an increased frequency of heat extremes over the contiguous U.S. However, some model-to-model differences are also found. For example, while the increased heat extreme frequency mainly occurs in the West and the South in CAM5 (Figure 3e), CAM6 composite analysis shows a northward shifted impact, particularly over the Pacific Northwest (Figure 4e). Also, despite the similarity in SST composite, the impact of eastern tropical Pacific cooling on U.S. heat extremes is slightly larger in the Northeast in CAM6 compared to CAM5 (Figures 3f and 4f). The associated wave train simulated in CAM6 also differs slightly from observations and CAM5 as the Aleutian low anomaly is shifted westward (Figure 4b).

Finally, we also perform similar composite analysis based on the ERA5 reanalysis (Figure 5). The results are mainly consistent with the LRF and prescribed SST experiments although the statistically significant regions are limited due to the small sample size. Differences lie in that, for example, in the western North Pacific warming composite, the associated increased heat extreme frequency is more confined to the west of the U.S. with a small decrease in the east (Figure 5e). In the eastern tropical Pacific cooling composite, while some limited significant increased heat extremes are seen in the Northeast and Midwest, decreased extremes are found in the west (Figure 5f).
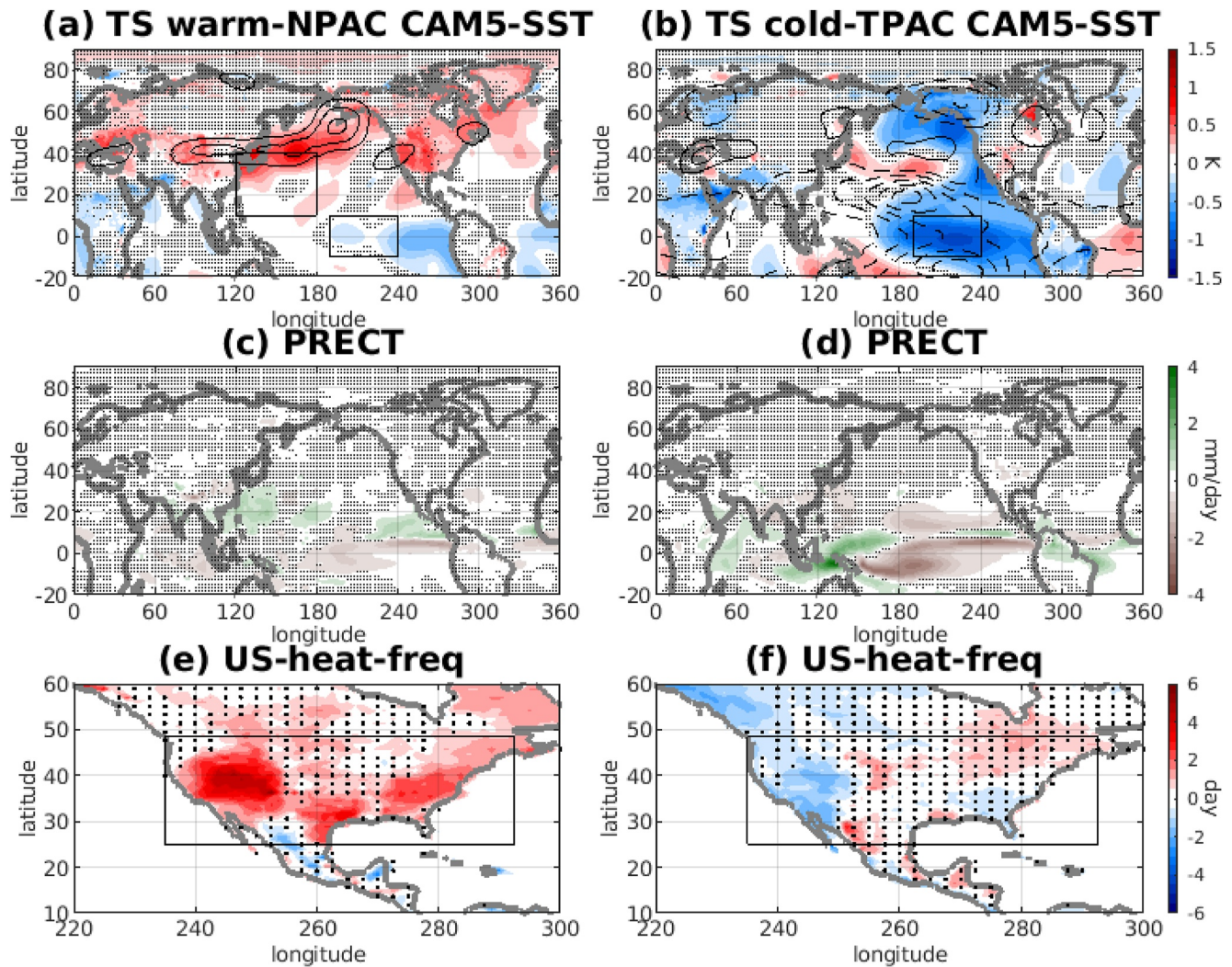
Figure 3. Composite of surface temperature, precipitation and U.S. heat extreme frequency anomalies from CAM5 prescribed SST experiments. June-July-August (a) surface temperature (color shadings) and 200 hPa geopotential height (contours), (c) precipitation and (e) U.S. heat extreme frequency anomalies associated with a warmer-than-normal western North Pacific (i.e., box-averaged temperature larger than 0.5 standard deviation) and a normal eastern tropical Pacific surface temperature (i.e., box-averaged temperature within ±0.5 standard deviation). Panels (a, c, e) are the average of 60 years (see Text S1 in Supporting Information S1 for detailed information). Panels (b, d, f) are similar but are associated with a colder-than-normal eastern tropical Pacific (i.e., box-averaged temperature less than −1 standard deviation) and are the average of 70 years (see Text S1 in Supporting Information S1 for detailed information). In (a) (b), solid contours indicate positive values and dashed contours indicate negative values. The contours in (a) start from 15 m with an interval of 5 m and in (b) start from 5 m with an interval of 5 m. Boxes in (a) indicate western North Pacific (120°–180°E, 10°–40°N) and eastern tropical Pacific (190°–240°E, 10°S–10°N), respectively. Box in (b) indicates eastern tropical Pacific. Box in (e, f) indicates the contiguous U.S. Dots indicate that the results are statistically insignificant at the 95% level and are plotted at every other grid point for better visualization.

4. Conclusion and Discussions

In this study we make use of the CAM5 Green's function q-flux perturbation experiments and explore the most effective remote oceanic q-flux that drives summertime U.S.-wide heat extremes. We find that q-flux warming of SSTs over the western North Pacific Ocean is the most effective in causing an increased heat extreme frequency via driving increased precipitation over the western North Pacific Ocean and an eastward propagating Rossby wave train, resulting in a ridge anomaly over the contiguous U.S. In comparison, q-flux cooling over the eastern tropical Pacific drives an increased heat extreme frequency but is less effective. Furthermore, guided by the LRF results, we separate the role of western North Pacific warming in the absence of eastern tropical Pacific cooling and eastern tropical Pacific cooling on U.S. heat extremes in prescribed SST experiments and the ERA5 reanalysis data set. Overall, consistent conclusions are found in both CAM5 and CAM6
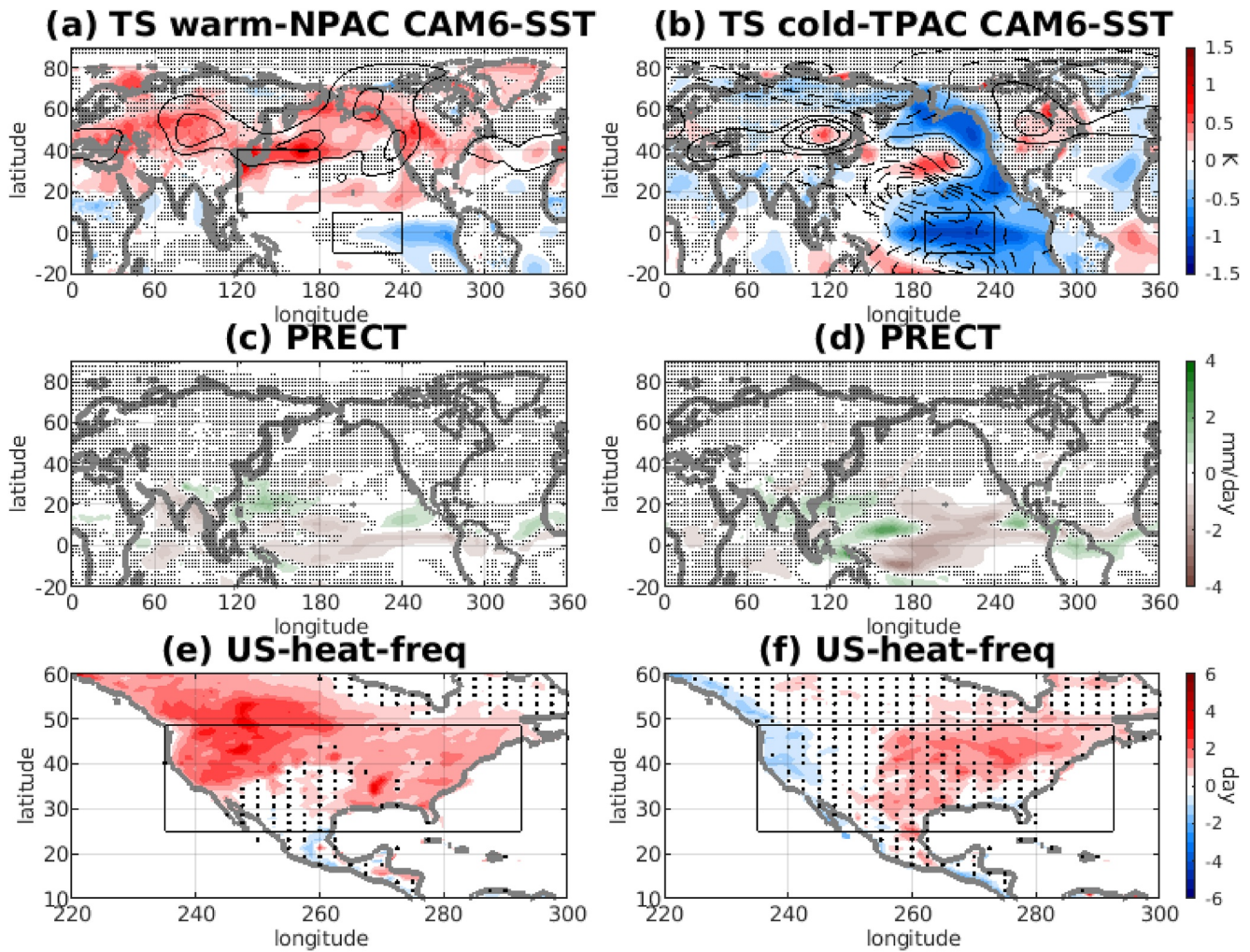
Figure 4. Similar to Figure 3 but for CAM6 prescribed SST experiments. Panels (a, c, e) are the average of 90 years. Panels (b, d, f) are the average of 80 years. For the composite years, see Text S1 in Supporting Information S1 for detailed information.

prescribed SST experiments and ERA5 although some model-to-model differences are noticed and the sample size is limited in ERA5.

By using novel Green's function experiments, we are able to separate the role of western North Pacific warming in the absence of eastern tropical Pacific cooling versus eastern tropical Pacific cooling on U.S. heat extremes. Our finding that the western North Pacific is the more efficient area is supported to some extent by the observations-based analysis. This has important implications for the predictability of U.S. heat extremes based on these remote precursors in SST. However, since we analyze summertime SSTs in both the tropical Pacific and western North Pacific regions, it is possible that if there is delayed effect of the tropical Pacific on the western North Pacific (e.g., B. Wang et al. (2001)), and our current analysis of the Green's function and prescribed SST experiments may not be able to capture the effect. We also note that we focus on the linear component of the response in this study but the nonlinear component could be non-negligible according to Lu et al. (2020). Also we rely on the Green's function experiments performed by a single atmospheric model given the availability of daily variables for the calculation of extremes. To explore possible model-to-model differences, the currently ongoing Green's Function Model Intercomparison Project could be the next step. Future work will also extend to other AMIP ensembles and coupled ocean-atmosphere simulations.
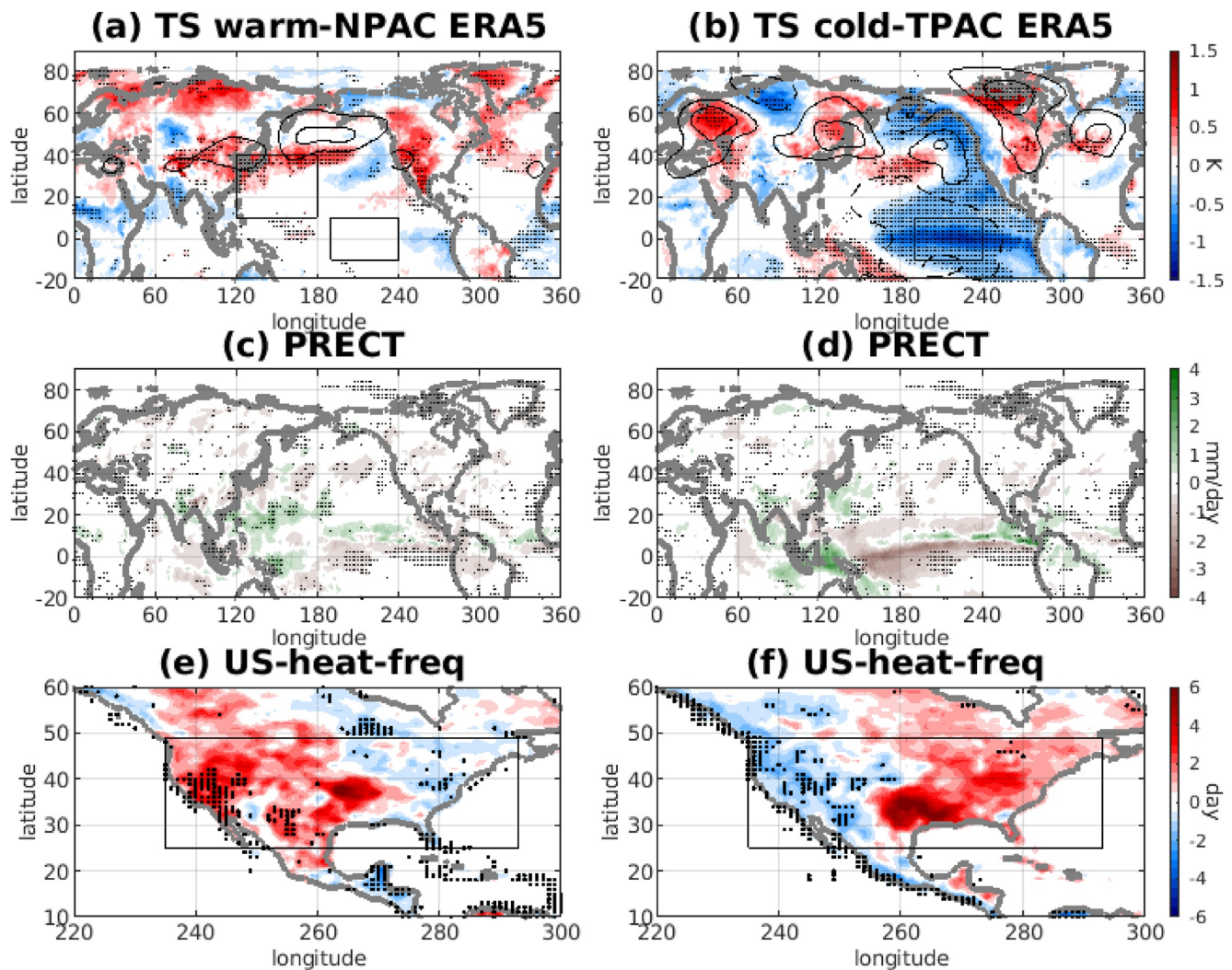
Figure 5. Similar to Figure 3 but for the ERA5 reanalysis. The left column is the composite mean of 9 years and the right column is based on 8 years. For the composite years, see Text S1 in Supporting Information S1 for detailed information. Dots indicate that the results are statistically significant at the 90% level.

Data Availability Statement

The CAM5 Green's function model output data used for the analysis in the study are available at Columbia University Academic Commons via (Wu, 2023). The ERA5 reanalysis data set is downloaded from the Copernicus Climate Change Service (C3S) Climate Date Store - https://cds.climate.copernicus.eu/#!/search?text=ERA5&type=dataset. The CAM5 prescribed SST model output is downloaded from https://www.cesm.ucar.edu/working-groups/climate/simulations/cam5-prescribed-sst. The CAM6 prescribed SST model output is downloaded from https://www.cesm.ucar.edu/working-groups/climate/simulations/cam6-prescribed-sst.

References

Barsugli, J. J., & Sardeshmukh, P. D. (2002). Global atmospheric sensitivity to tropical SST anomalies throughout the Indo-Pacific basin. *Journal of Climate*, *15*(23), 3427–3442. https://doi.org/10.1175/1520-0442(2002)015<3.427:GASTTS>2.0.CO;2

Deng, K., Ting, M., Yang, S., & Tan, Y. (2018). Increased frequency of summer extreme heat waves over Texas area tied to the amplification of Pacific zonal SST gradient. *Journal of Climate*, *31*(14), 5629–5647. https://doi.org/10.1175/jcli-d-17-0554.1

Ding, Q., Wang, B., Wallace, J. M., & Branstator, G. (2011). Tropical–extratropical teleconnections in boreal summer: Observed interannual variability. *Journal of Climate*, *24*(7), 1878–1896. https://doi.org/10.1175/2011JCLI3621.1

Dole, R., Hoerling, M., Perlwitz, J., Eischeid, J., Pegion, P., Zhang, T., et al. (2011). Was there a basis for anticipating the 2010 Russian heat wave? *Geophysical Research Letters*, *38*(6), L06702. https://doi.org/10.1029/2010GL046582

Donat, M. G. E. A., King, A. D., Overpeck, J. T., Alexander, L. V., Durre, I., & Karoly, D. J. (2016). Extraordinary heat during the 1930s US Dust Bowl and associated large-scale conditions. *Climate Dynamics*, *46*(1–2), 413–426. https://doi.org/10.1007/s00382-015-2590-5

Dong, Y., Proistosescu, C., Armour, K. C., & Battisti, D. S. (2019). Attributing historical and future evolution of radiative feedbacks to regional warming patterns using a Green's function approach: The preeminence of the western Pacific. *Journal of Climate*, *32*(17), 5471–5491. https://doi.org/10.1175/JCLI-D-18-0843.1

Fischer, E. M., Seneviratne, S. I., Vidale, P. L., Luthi, D., & Schar, C. (2007). Soil moisture–atmosphere interaction during the 2003 European summer heat wave. *Journal of Climate*, *20*, 5081–5099. https://doi.org/10.1175/JCLI4288.1

Goodman, J. C., & Marshall, J. (2002). Using neutral singular vectors to study low-frequency atmospheric variability. *Journal of the Atmospheric Sciences*, *59*(22), 3206–3222. https://doi.org/10.1175/1520-0469(2002)059<3206:UNSVTS>2.0.CO;2

Gritsun, A. (2010). Construction of the response operators to small external forcings for atmospheric general circulation atmospheric models with time periodic right-hand sides. *Izvestiya - Atmospheric and Oceanic Physics*, *46*(6), 748–756. https://doi.org/10.1134/S000143381006006X

Hassanzadeh, P., & Kuang, Z. (2016). The linear response function of an idealized atmosphere. Part I: Construction using Green's functions and applications. *Journal of the Atmospheric Sciences*, *73*(9), 3423–3439. https://doi.org/10.1175/JAS-D-15-0338.1

Hersbach, H., Bell, B., Berrisford, E. A. P., Hirahara, S., Horányi, A., Muñoz-Sabater, J., et al. (2020). The ERA5 global reanalysis. *Quarterly Journal of the Royal Meteorological Society*, *146*(730), 1999–2049. https://doi.org/10.1002/qj.3803

Hoerling, M., & Kumar, A. (2003). The perfect ocean for drought. *Science*, *299*(5607), 691–694. https://doi.org/10.1126/science.1079053

Hurrell, J. W., Holland, M. M., Gent, P. R., Ghan, S., Kay, J. E., Kushner, P. J., et al. (2013). The community Earth system model: A framework for collaborative research. *Bulletin of the American Meteorological Society*, *94*(9), 1339–1360. https://doi.org/10.1175/BAMS-D-12-00121.1

Jong, B.-T., Ting, M., Seager, R., & Anderson, W. B. (2020). ENSO teleconnections and impacts on U.S. summertime temperature during a multiyear La Nina life cycle. *Journal of Climate*, *33*(14), 6009–6024. https://doi.org/10.1175/JCLI-D-19-0701.1

Lau, N.-C., Leetmaa, A., Nath, M. J., & Wang, H.-L. (2005). Influences of ENSO-induced Indo-western Pacific SST anomalies on extratropical atmospheric variability during the boreal summer. *Journal of Climate*, *18*(15), 2922–2942. https://doi.org/10.1175/JCLI3445.1

Lee, Y.-Y., & Grotjahn, R. (2019). Evidence of specific MJO phase occurrence with summertime California central valley extreme hot weather. *Advances in Atmospheric Sciences*, *36*(6), 589–602. https://doi.org/10.1007/s00376-019-8167-1

Lin, H., Mo, R., & Vitart, F. (2022). The 2021 western North American heatwave and its subseasonal predictions. *Geophysical Research Letters*, *49*(6), e2021GL097036. https://doi.org/10.1029/2021GL097036

Liu, F., Lu, J., Garuba, O., Leung, L. R., Luo, Y., & Wan, X. (2018). The sensitivity of surface temperature to oceanic forcing via q-flux Green's function experiments. Part I: Linear response function. *Journal of Climate*, *31*(9), 3625–3641. https://doi.org/10.1175/JCLI-D-17-0462.1

Lopez, H., Kim, D., West, R., & Kirtman, B. (2022). Modulation of North American heat waves by the tropical Atlantic warm pool. *Journal of Geophysical Research: Atmospheres*, *127*(21), e2022JD037705. https://doi.org/10.1029/2022JD037705

Lopez, H., Lee, S. K., Dong, S., Goni, G., Kirtman, B., Atlas, R., & Kumar, A. (2019). East Asian monsoon as a modulator of U.S. Great Plains heat waves. *Journal of Geophysical Research: Atmospheres*, *124*(12), 6342–6358. https://doi.org/10.1029/2018JD030151

Lorenz, R., Jaeger, E. B., & Seneviratne, S. I. (2010). Persistence of heat waves and its link to soil moisture memory. *Geophysical Research Letters*, *37*(9), L09703. https://doi.org/10.1029/2010GL042764

Lu, J., Liu, F., Leung, L. R., & Lei, H. (2020). Neutral modes of surface temperature and the optimal ocean thermal forcing for global cooling. *NPJ Climate and Atmospheric Science*, *3*(1), 9. https://doi.org/10.1038/s41612-020-0112-6

Lyon, B., & Dole, R. M. (1995). A diagnostic comparison of the 1980 and 1988 US summer heat wave-droughts. *Journal of Climate*, *8*(6), 1658–1675. https://doi.org/10.1175/1520-0442(1995)008<1658:adcota>2.0.co;2

Marshall, J., & Molteni, F. (1993). Toward a dynamical understanding of planetary-scale flow regimes. *Journal of the Atmospheric Sciences*, *50*(12), 1792–1818. https://doi.org/10.1175/1520-0469(1993)050<17.92:TADUOP>2.0.CO;2

McKinnon, K. A., Rhines, A., Tingley, M. P., & Huybers, P. (2016). Long-lead predictions of eastern United States hot days from Pacific sea surface temperatures. *Nature Geoscience*, *9*(5), 389–394. https://doi.org/10.1038/ngeo2687

Meehl, G. A., & Tebaldi, C. (2004). More intense, more frequent, and longer lasting heat waves in the 21st century. *Science*, *305*(5686), 994–997. https://doi.org/10.1126/science.1098704

Mueller, B., & Seneviratne, S. I. (2012). Hot days induced by precipitation deficits at the global scale. *Proceedings of the National Academy of Sciences of the United States of America*, *109*(31), 12398–12403. https://doi.org/10.1073/pnas.1204330109

Namias, J. (1982). Anatomy of Great Plains protracted heat waves (especially the 1980 US summer drought). *Monthly Weather Review*, *110*(7), 824–838. https://doi.org/10.1175/1520-0493(1982)110<0824:aogpph>2.0.co;2

Namias, J. (1991). Spring and summer 1988 drought over the contiguous United States - Causes and prediction. *Journal of Climate*, *4*(1), 54–65. https://doi.org/10.1175/1520-0442(1991)004<0054:sasdot>2.0.co;2

Palmer, T. N. (1999). A nonlinear dynamical perspective on climate prediction. *Journal of Climate*, *12*(2), 575–591. https://doi.org/10.1175/1520-0442(1999)012<0575:ANDPOC>.2.0.CO;2

Perkins-Kirkpatrick, S. E., & Lewis, S. C. (2020). Increasing trends in regional heatwaves. *Nature Communications*, *11*(1), 3357. https://doi.org/10.1038/s41467-020-16970-7

Petoukhov, V., Rahmstorf, S., Petri, S., & Schellnhuber, H. J. (2013). Quasi-resonant amplification of planetary waves and recent Northern Hemisphere weather extremes. *Proceedings of the National Academy of Sciences of the United States of America*, *110*(14), 5336–5341. https://doi.org/10.1073/pnas.1222000110

Schnell, J. L., Prather, M. J., Josse, B., Naik, V., Horowitz, L. W., Zeng, G., et al. (2016). Effect of climate change on surface ozone over North America, Europe, and East Asia. *Geophysical Research Letters*, *43*(7), 3509–3518. https://doi.org/10.1002/2016GL068060

Schubert, S. D., Suarez, M. J., Pegion, P. J., Koster, R. D., & Bacmeister, J. T. (2004). On the cause of the 1930s dust bowl. *Science*, *303*(5665), 1855–1859. https://doi.org/10.1126/science.1095048

Screen, J. A., & Simmonds, I. (2014). Amplified mid-latitude planetary waves favour particular regional weather extremes. *Nature Climate Change*, *4*(8), 704–709. https://doi.org/10.1038/nclimate2271

Shen, L., Mickley, L. J., & Gilleland, E. (2016). Impact of increasing heat waves on US ozone episodes in the 2050s: Results from a multimodel analysis using extreme value theory. *Geophysical Research Letters*, *43*(8), 4017–4025. https://doi.org/10.1002/2016gl068432

Teng, H., Branstator, G., Wang, H., Meehl, G. A., & Washington, W. M. (2013). Probability of US heat waves affected by a subseasonal planetary wave pattern. *Nature Geoscience*, *6*(12), 1056–1061. https://doi.org/10.1038/ngeo1988

Trenberth, K. E., & Fasullo, J. T. (2012). Climate extremes and climate change: The Russian heat wave and other climate extremes of 2010. *Journal of Geophysical Research*, *117*(D17), D17103. https://doi.org/10.1029/2012JD018020

Wang, B., Wu, R., & Lau, K.-M. (2001). Interannual variability of the Asian summer monsoon: Contrasts between the Indian and the western North Pacific–East Asian monsoons. *Journal of Climate*, *14*(20), 4073–4090. https://doi.org/10.1175/1520-0442(2001)014<4073:ivotas>2.0.co;2

Wang, H., Schubert, S., Koster, R., Ham, Y.-G., & Suarez, M. (2014). On the role of SST forcing in the 2011 and 2012 extreme U.S. heat and drought: A study in contrasts. *Journal of Hydrometeorology*, *15*(3), 1255–1273. https://doi.org/10.1175/JHM-D-13-069.1

Williams, P. A., Allen, C., Macalady, A. E. A., Griffin, D., Woodhouse, C. A., Meko, D. M., et al. (2013). Temperature as a potent driver of regional forest drought stress and tree mortality. *Nature Climate Change*, *3*, 292–297. https://doi.org/10.1038/nclimate1693

Wu, Y. (2023). Data: The most effective remote forcing in causing U.S.-wide heat extremes as revealed by CESM Green's function experiments [Dataset]. Columbia University Academic Commons. https://doi.org/10.7916/r4xt-3p80

Wu, Y., Lu, J., Ding, Q., & Liu, F. (2021). Linear response function reveals the most effective remote forcing in causing September Arctic sea ice melting in CESM. *Geophysical Research Letters*, *48*(15), e2021GL094189. https://doi.org/10.1029/2021GL094189

Zhu, Z., & Li, T. (2016). A new paradigm for continental U.S. summer rainfall variability: Asia–North America teleconnection. *Journal of Climate*, *29*(20), 7313–7327. https://doi.org/10.1175/JCLID-16-0137.1